

The three phases of self-gravitating scalar field ground states

Anthony E. Mirasola,¹ Nathan Musoke,² Mark C. Neyrinck,³ Chanda Prescod-Weinstein,² and J. Luna Zagorac⁴

¹*Department of Physics University of Illinois at Urbana-Champaign Urbana, IL 6180, USA*

²*Department of Physics & Astronomy University of New Hampshire Durham, NH 03824, USA*

³*Blue Marble Space Institute of Science, Seattle, WA 98104, USA*

⁴*Perimeter Institute for Theoretical Physics 31 Caroline St. N. Waterloo, ON N2L2Y5, Canada*

(Dated: October 31, 2024)

It is generally assumed that scalar field dark matter halos would contain *solitonic cores*—spherically symmetric ground state configurations—at their centers. This is especially interesting in the case of ultralight dark matter (ULDM), where the solitons sizes are on the order of galaxies. In this work, we show that the paradigm of a spherically symmetric soliton embedded in the center of each halo is not universally valid in a scenario with multiple interacting scalar fields. In particular, sufficiently strong repulsive interspecies interactions make the fields immiscible. In such models, the ground state configuration can fall into a number of different phases that depend on the fields' relative densities, masses, and interaction strengths. This raises the possibility that the inner regions of ULDM halos are more complex and diverse than previously assumed.

Introduction Gravitating scalar fields are important components of theoretical models in cosmology. They arise naturally from certain overarching theories of quantum gravity and can have a variety of observational consequences in the Universe, including as ultralight dark matter (ULDM) [1], and in models of inflation [2–5]. In this letter, we discuss the ground states and equilibria of one family of real scalar fields.

In scalar ULDM scenarios, the wave-like nature of the field becomes consequential on larger spatial scales set by the de Broglie wavelength, $\lambda_{\text{dB}} \propto m^{-1}$. They form Bose-Einstein condensates on this scale. For a particle mass of $m \sim 10^{-19} - 10^{-22}$, the de Broglie wavelength becomes evident on galactic scales ($\lambda_{\text{dB}} \sim 1$ kpc) when the particle has no non-gravitational interactions [6].

Most work on ULDM assumes that each dark matter halo has a *solitonic core* at its center. In ULDM, solitons condense quickly enough that most halos would contain a soliton [7–13]. The role solitons could play as a solution to the cusp-core problem contributed to ULDM rising in popularity as a dark matter candidate [14, 15]. While recent work has investigated the relative size and shape of solitonic cores in simulated ULDM halos [16–22], their existence in centers of halos has not been called into question. Nevertheless, the string axiverse generically predicts the existence of multiple ultralight fields with nonzero self- and interspecies interactions [23, 24], which in turn impacts the core profiles of such structures [25]. Therefore, the mapping from interaction strengths to core profiles to the diversity of halos found in nature could enable constraints on axiverse models.

These results also have implications for inflation. In some inflationary models, the reheating epoch is analogous to structure formation in ULDM [26, 27], going as far as the formation of inflaton halos and solitonic inflaton stars [8]. Interactions between multiple scalar inflaton fields would significantly change these collapsed states, impacting their dynamics during reheating and

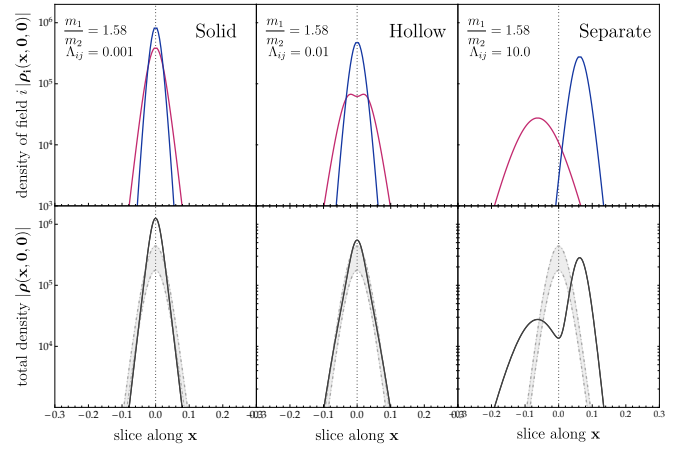


FIG. 1. Illustrations of the three classes of ground state configurations discussed in this paper. Each panel shows a slice through the center of a 3D simulation box. Upper panels show the densities of the individual fields; lower panels show the corresponding total density. For comparison, single-field solitons of equivalent total and particle masses are shown in light gray. **The existence of three distinct classes of ground states and the resulting diversity in halo density shapes is the main result of this work.**

the consequent observational predictions [28].

We present a detailed analysis of the equilibria of two-species models with interspecies interactions. We find that there is a wider variety of possible equilibria than previously known. In particular, we find that sufficiently repulsive interactions would imply immiscible phases, mimicking immiscible behavior that occurs in dual species Bose-Einstein condensates of ultracold atoms [29–35]. Even under the assumption of spherical symmetry, sufficiently repulsive interactions imply the existence of ground states in which the maxima of the two species are not co-located. Upon relaxing the assumption of spherical symmetry, we find that ground states

are not necessarily spherically symmetric. This picture would become increasingly complex with more than two species of scalar particles. This is, to our knowledge, the first instance of non-spherically symmetric ground states in cosmological scalar fields.

Background Multispecies ULDM is governed by a system of coupled Gross-Pitaevskii-Poisson (GPP) equations:

$$i\hbar\frac{\partial\psi_j}{\partial t} = -\frac{\hbar^2}{2m_j}\nabla^2\psi_j + m_j\Phi\psi_j + \frac{\hbar^3}{2m_j^2}\lambda_{jj}|\psi_j|^2\psi_j + \frac{\hbar^3}{4m_j^2}\sum_k\lambda_{jk}|\psi_k|^2\psi_j \quad (1)$$

$$\nabla^2\Phi = 4\pi G\sum_j m_j|\psi_j|^2 \quad (2)$$

where Φ is the Newtonian gravitational potential, and the indices j, k run over the N fields considered, each with particle mass m_j . The self- and interspecies interactions are parameterized by a symmetric matrix λ_{jk} with positive (negative) values corresponding to repulsive (attractive) interactions. The GPP equations arise from the Newtonian limit of the ULDM Lagrangian [25].

The mass density of each species is

$$\rho_j(\mathbf{x}, t) = m_j|\psi_j(\mathbf{x}, t)|^2, \quad (3)$$

and the total mass in each field is independently conserved.

The conserved energy of equations (1) and (2) is

$$E = E_{\text{grav}} + E_{\text{KQ}} + \sum_j E_{\text{self}}^j + \sum_j \sum_k E_{\text{int}}^{j,k} \quad (4)$$

where the gravitational potential energy is

$$E_{\text{grav}} = \int d\mathbf{x}^3 \frac{1}{2}\Phi \sum_j m_j|\psi_j|^2. \quad (5)$$

The total kinetic energy consists of a classical term (arising from bulk motion) and quantum term.¹ Throughout this work we only consider equilibria, so the classical kinetic energy is zero and the total kinetic energy will be equal to the quantum kinetic energy:

$$E_{\text{KQ}} = \frac{\hbar^2}{2} \int d\mathbf{x}^3 \sum_j \frac{1}{m_j} |\nabla\psi_j|^2 \quad (6)$$

The energies due to self-interactions and inter-field interactions respectively are

$$E_{\text{self}}^j = \frac{\hbar^3\lambda_{jj}}{2m_j^2} \int d\mathbf{x}^3 |\psi_j|^4; E_{\text{int}}^{j,k} = \frac{\hbar^3\lambda_{jk}}{2m_j^2} \int d\mathbf{x}^3 |\psi_k|^2 |\psi_j|^2. \quad (7)$$

¹ Note that the ‘‘quantum’’ kinetic energy does not have a quantum origin, but simply refers to the kinetic energy that does not correspond to any bulk motion [36].

In our investigations of the conditions of the system’s immiscibility—or separation of ground states, as presented in the rightmost panel of Fig. 1—we will make particular use of the energy definitions above. Our units and code used are defined in the Appendix.

Analytic evidence for phase transitions Before solving our system numerically, we present derivations of exact expressions for the energies under a spherically symmetric Gaussian ansatz for the ground state profiles. For single-species ULDM solitons, this ansatz has close agreement with numerical solutions [37, 38]. We assume each field has the profile defined by its mass M_i and length scale R_i , with centres of the profiles separated by a distance d :

$$\rho_i(\mathbf{r}) = \frac{M_i}{\pi^{3/2}R_i^3} \exp[-r^2/R_i^2]. \quad (8)$$

With this ansatz, we can find analytic expressions for the quantum kinetic, gravitational, and interaction energies. As mentioned above, the quantum kinetic energy does not depend on the separation distance d , and therefore plays no role in determining which phase is preferred. The interaction energy can be calculated from Eq. (7),

$$E_{\text{int}}^{12}(d) = \frac{\hbar^3\lambda_{12}}{4\mu^2} \frac{M_1M_2}{\pi^{3/2}(R_1^2 + R_2^2)^{3/2}} \exp\left[-\frac{d^2}{R_1^2 + R_2^2}\right], \quad (9)$$

where $\mu^2 = m_1^2m_2^2/(m_1^2 + m_2^2)$. The gravitational energy has a self-gravitational component and interspecies gravitational component. The former is independent of d and is easily calculated as

$$E_{\text{grav}}^i = \int d^3\mathbf{r} \rho_i(\mathbf{r})\Phi_i(\mathbf{r}) = \frac{-1}{\sqrt{2\pi}} \frac{GM_i^2}{R_i}, \quad (10)$$

where Φ_i denotes the gravitational potential generated by species i . To calculate the interspecies gravitational energy E_{grav}^{12} , we consider two cases. First when $d = 0$, we can calculate it exactly in the Gaussian ansatz,

$$E_{\text{grav}}^{12}(d=0) = \int d^3\mathbf{r} (\rho_1\Phi_2 + \rho_2\Phi_1) \quad (11)$$

$$= \frac{2GM_1M_2}{\sqrt{\pi}} \left[\frac{1}{\sqrt{R_1^2 + R_2^2}} - \frac{R_1^2}{(R_1^2 + R_2^2)^{3/2}} - \frac{R_2^2}{(R_1^2 + R_2^2)^{3/2}} \right]. \quad (12)$$

A simplification occurs when the two species have equal total mass M , particle mass m , and radii R . In this case the total gravitational energy evaluates to

$$E_{\text{grav}}(d=0) = \frac{-4}{\sqrt{2\pi}} \frac{GM^2}{R}. \quad (13)$$

This agrees with the total gravitational energy of a single-species soliton in the Gaussian ansatz.

Second, at finite separation distance $d > 0$, the interspecies gravitational energy E_{grav}^{12} must be evaluated numerically. However, it can be approximated at large separation distances $d \gg R_1, R_2$ by noting that in this case the solitons become effectively point masses such that

$$E_{\text{grav}}^{12}(d \gg R_i) = \frac{-GM_1M_2}{d}. \quad (14)$$

The gravitational energy E_{grav} and the energy E_{int} due to repulsive interactions are in competition with each other: E_{grav} is minimized at $d = 0$, while E_{int} is minimized at $d = \infty$. This suggests that there is a critical interaction strength at which the energy minimizing separation distance changes from $d = 0$ to $d > 0$. We can estimate the critical interaction strength λ_{12}^* by comparing the total energy at $d = 0$ to the total energy at $d = \infty$, $\Delta E = E(d = 0) - E(d = \infty)$. Since the quantum kinetic energy and self-gravitational energies are independent of d and both interspecies gravitational energy and interaction energy go to zero as d becomes infinite, this simplifies to $\Delta E = E_{\text{int}}(d = 0) + E_{\text{grav}}^{12}(d = 0)$. When ΔE is positive, the system has lower total energy at infinite separation distance than at zero separation distance, indicating that the system is not in the nested miscible phase. Thus, solving $\Delta E = 0$ gives an estimate for the critical interaction strength. When the two species have equal total mass and particle mass, this results in

$$\lambda_{12}^* \approx \frac{8\pi GR^2 m^2}{\hbar^3}. \quad (15)$$

The radius R can be determined by variationally minimizing the energy of the Gaussian ansatz. Fixing to zero separation distance, this results in

$$R = \frac{3\sqrt{\pi}\hbar^2}{4\sqrt{2}GMm^2} \left(1 + \sqrt{1 + \frac{GM^2 m^2 \lambda_{12}^*}{6\pi^2 \hbar}} \right). \quad (16)$$

Together with Eq. (15), this allows us to estimate the critical interaction strength for a given total mass. For two fields of particle mass $m = 1$, and soliton mass $M = 50$, this results in an estimated critical interaction strength of $\lambda_{12}^* = 0.09$. This closely approximates the critical interaction strength we observe in numerical simulations presented below, where we find $\lambda_{12}^* = 0.1$.

Numerical results and phase diagram Having established an expectation for a critical interspecies interaction value λ_{12}^* where a phase transition will occur, we now relax our Gaussian ansatz to find more realistic ground state profiles. For a single self-gravitating scalar field, the ground state profile is called a *soliton*. Solitons are static spherically symmetric states with balanced gravitational and “quantum”/gradient forces. The density profile of a single-field soliton without self-interactions is well-approximated as

$$\rho(r) = \frac{\rho_s}{\left(1 + (r/r_s)^2\right)^8}, \quad (17)$$

where ρ_s is the central density and the scale radius is

$$r_s \simeq 0.335 \frac{10^9 M_\odot}{M} \left(\frac{10^{-22} \text{eV}}{m} \right)^2 \text{ kpc}. \quad (18)$$

The total mass of this profile is

$$M = 2.2 \times 10^8 \left(\frac{m}{10^{-22} \text{eV}} \right)^{-2} \left(\frac{r_s}{\text{kpc}} \right)^{-1} M_\odot. \quad (19)$$

The radius of a soliton decreases with both the mass m of its constituent particles and its total mass M .

In realistic halos, the situation becomes more complicated. Solitons in power-law backgrounds are well approximated by changing the scale radius and exponent of -8 in equation (17) [39, 40]. Self-interactions in single field ULDM affect the possible types of equilibria and imply maximum soliton masses [41].

The profile of a non-isolated ground state is even more complex than equation (17)—in addition to m_j and M_j , the field ψ_j depends on the other fields $\psi_{k \neq j}$. Although the exact dependence is nontrivial, the overall trend of $r_s \propto m_j^{-2} M_j^{-1}$ is preserved [42]. When $\lambda_{ij} = 0$, the only interspecies feedback is through the gravitational field, and so multi-species equilibria are essentially multiple coincident single-field solitons, scaled to account for a background gravitational field. Therefore, it makes sense that previous work on equilibria of multi-species scalar fields has assumed spherical symmetry and coincident centers of mass [25, 43–46]. In keeping with previous literature, we will call such configurations *nested* [47].

Here, we take the final step by assuming $\lambda_{ij} > 0$ and finding the ground states of such systems numerically. We use a Mathematica module named `nSPIRa1` to find numerical solutions with multiple species and self-interactions. `nSPIRa1` is an extension of the code used in Ref. [48] to evolve the spherically symmetric version of the Schrödinger-Poisson system in time. Unlike the previous version, `nSPIRa1` allows for multiple axion fields, self- and inter-field interactions, and the choice of real or imaginary time. In this work, we use it to evolve the spherically symmetric equations of motion for two fields forward in imaginary time to arrive at the overall system’s ground state; see the Appendix for more details.

We find this to be a reasonable approach for the following reasons. Our initial guess for each wavefunction is some superposition of eigenstates of the system. Each eigenstate has an associated eigenenergy, with the ground state having the lowest energy. If we ignore the backreaction on the gravitational potential for a moment, each wavefunction ψ_j will evolve as

$$\psi_j(t) = \sum_{i=1}^N c_j^i \exp\left(-iE_j^i t\right) \phi_j^i, \quad (20)$$

where ϕ_j^i is an eigenstate, E_j^i its associated eigenenergy, and c_j^i a complex expansion coefficient. Now, evolving in

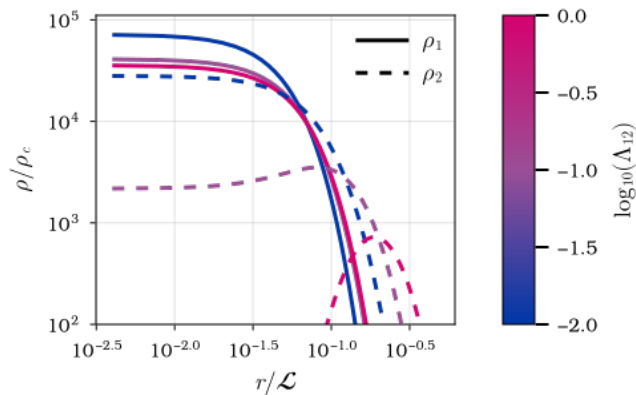


FIG. 2. Density profiles of numerically calculated spherically symmetric ground states. The solid lines are densities of ψ_1 and the dashed lines are densities of ψ_2 . The color scale indicates the interaction strength λ_{12} ; large positive values are repulsive. In each case, $M_1 = M_2 = 50M$, $m_1 = m_0$ and $m_2 = 10^{-0.1}m_0$. When the interaction strength is small, solutions are nested, similar to those presented in figure 4 and discussed elsewhere in the literature. The less massive field ψ_2 has a larger characteristic radius, as expected from equation (17). When interactions are strongly repulsive, we find hollow solutions, in which ψ_2 has a local minimum at $r = 0$.

imaginary time $r \rightarrow it$ causes the exponential to decay at a rate set by E_j^i . Given the ground state has the largest energy, excited states will exponentially decay first, leaving us with the ground state profile.

For each simulation, we must first specify initial conditions for the ψ_j profiles; we use the multifield solitons described in [25]. We have found that much of our parameter space is relatively insensitive to changes in these three parameters; however, choosing them becomes crucial when $m_1 = m_2$ and $M_1 = M_2$. In this case, the imaginary time evolution preserves the symmetry $\psi_1(r) = \psi_2(r)$, and only nested soliton-like solutions are found. It is possible to find solutions that violate this symmetry by starting with $\psi_1(r) \neq \psi_2(r)$. The choice of initial conditions becomes important in this region, as the ground states of the two fields become very nearly degenerate (or exactly degenerate in the case of $m_1 = m_2$ and $M_1 = M_2$). We thus find a set of solutions that are still nested, but now no longer have coincident maxima; we call this type of solution *nested hollow*, and the type described above *nested solid* for disambiguation. The transition from solid to hollow profiles with increasing λ_{ij} is illustrated in Fig. 2.

We construct a phase diagram by testing a range of parameters λ_{ij} , m_1/m_2 , and M_1/M_2 . In the region where the fields are nearly degenerate, we verify that we have reached the true ground state by running several choices of initial conditions and choosing the one that minimizes the energy of the system. The results are shown in Fig. 3.

Having identified two miscible yet qualitatively different states, we now recall that analytic arguments pre-

sented in the last section support a third: an immiscible phase we call *separate*, where the centers of mass of the two scalar field solitons are separated by a distance d . Such a configuration breaks spherical symmetry, and is therefore beyond the reach of our 1D imaginary time solver; however, we can use energy arguments to find the transition parameters instead. Recall that the gravitational potential energy consists of contributions from the self-gravitating configurations of each scalar field and a two-body term. The two-body gravitational energy is minimized when $d = 0$, while the interaction energy is minimized as $d \rightarrow \infty$. The quantum kinetic energy is agnostic with respect to the two fields' centers of mass, but is minimized when both density profiles are solitonic; the self-gravitating terms behave similarly. Therefore, the *nested solid* state arises when gravitational and quantum kinetic energies are minimized at the expense of the interaction energy; the *nested hollow* state arises when the interaction energy is lowered at the expense of the quantum energy of one of the states (whichever is “hollow”); and the *separate* state arises when the interaction and quantum energies are minimized at $d > 0$ at the expense of the two-body gravitational energy.

Thus, we expect the transition from miscibility to immiscibility will occur approximately when the energy budget of the quantum, interaction, and self-gravity energies is on the order of the 2-body gravitational energy

$$E_{KQ} + E_{\text{int}} + \sum |E_{\text{grav}}^i| \sim |E_{\text{grav}}^{12}|. \quad (21)$$

Because the dependence of the energies on wavefunction profiles and their overlap cannot be fully disentangled from their dependence on the distance between the centers of mass, this argument cannot be easily leveraged to make analytic predictions on phase transitions. However, we include it here as useful intuition for why the three phases arise.

Furthermore, we verified the hollow phase is *not* just a numerical artifact of the 1D imaginary time solver by putting a range of corresponding wavefunction profiles on a 3D grid using `UltraDark.jl` [49]. For each case, we compared the energy of our profiles with the energy of two solitonic profiles of appropriate masses at different distances. For many cases classified as “Hollow 1” or “Hollow 2” in Fig. 3, the hollow phase did indeed minimize the total energy.

Three examples of energy-minimizing configurations verified in 3D are illustrated in Fig. 1. When the separate phase was preferred, we evaluated the energy of solitons at different distances $d > 0$ to find the value which minimizes the overall energy. This is how we arrived at the profile shown in the rightmost panel of Fig. 1. We also observed a general trend of the energy-minimizing distance d growing with increasing λ_{ij} . However, it should be noted that the total energy is very sensitive to numerical resolution, which is necessarily smaller in the 3D

simulations than their 1D counterparts. For this reason, careful construction of a full 3D phase diagram is relegated to work in our near future.

Discussion This work is a proof of concept that in scenarios with multiple gravitating scalar fields, there are at least three distinct phases which has phenomenological implications, including an immiscible phase. Work is ongoing to calculate ground states without the assumption of spherical symmetry. These calculations will allow a phase diagram to be constructed that includes the immiscible phase. Our work presented here indicates that relaxing the assumption of spherical symmetry results in the two fields separating into axially symmetric states; but with three or more fields even axial symmetry is broken in the immiscible phase. In general the structure of ground state configurations for n fields with self- and interspecies interactions can become very complicated.

Work to understand the phase diagram in such models is realistic and timely, as understanding the range of possible halo profiles in the axiverse could be confronted with data from current observational efforts constraining CDM. For example, the ongoing search for dark matter halos below $10^6 M_\odot$ is meant to test CDM’s prediction that halos are self-similar at all scales, but could be equivalently leveraged to impose limits on axiverse particle numbers and masses given a range of possible interaction strengths and, therefore, halo shapes.

Thus, in light of the increasing diversity of equilibria in scalar dark matter, we propose that “soliton” is no longer a sufficiently descriptive term for the cores predicted to exist in ULDM models. Not only can each field’s ground state differ from the solitonic profile approximated by Eq. 17 in terms of appropriate slope and radius r_s , one field in the nested hollow phase ceases resembling a core of any kind. Furthermore, there is some disagreement in the still nascent literature on whether solitons or cores even form in multi-species scenarios. Jain et al. [50] find that solitonic cores condense much more slowly when there are multiple fields—the condensation of one field serving to “frustrate” the efforts of the other—while Luu et al. [47] found that condensation can happen more quickly than in the case of a single field. The addition of non-gravitational interactions could either speed or slow this process further; either would have an effect on cosmological structure formation in the axiverse, and would therefore be testable with current and upcoming observational missions.

ACKNOWLEDGEMENTS

We thank Noah Glennon for discussions in the beginning stages of this project. LZ would like to thank Nikhil Padmanabhan for help setting up the code that would eventually evolve to become `nSPIRa1`. We thank the administrative and facilities staff at the University of New

Hampshire including Katie Makem-Boucher and Michelle Mancini.

Computations were performed on Marvin, a Cray CS500 supercomputer at UNH supported by the NSF MRI program under grant AGS-1919310. AEM’s contributions to this project were supported by DOE Grant DE-SC0020220. CPW’s contributions to this project were supported by the Research Corporation of America’s Cottrell Scholars program. This work was performed in part at Aspen Center for Physics, which is supported by National Science Foundation under Grant No. PHY-1607611. Research at Perimeter Institute is supported in part by the Government of Canada through the Department of Innovation, Science and Economic Development Canada and by the Province of Ontario through the Ministry of Colleges and Universities.

Appendix

Cosmology & Code Units

When performing numerical simulations, we use units defined according to a reference particle mass m_0 :

$$\mathcal{L} = \left(\frac{8\pi\hbar^2}{3m_0^2 H_0^2 \Omega_{m0}} \right)^{\frac{1}{4}} \approx 121 \left(\frac{10^{-23}\text{eV}}{m_0} \right)^{\frac{1}{2}} \text{ kpc}, \quad (22)$$

$$\mathcal{T} = \left(\frac{8\pi}{3H_0^2 \Omega_{m0}} \right)^{\frac{1}{2}} \approx 75.5 \text{ Gyr}, \quad (23)$$

$$\mathcal{M} = \frac{1}{G} \left(\frac{8\pi}{3H_0^2 \Omega_{m0}} \right)^{-\frac{1}{4}} \left(\frac{\hbar}{m_0} \right)^{\frac{3}{2}} \approx 7 \times 10^7 \left(\frac{10^{-23}\text{eV}}{m_0} \right)^{\frac{3}{2}} M_\odot \quad (24)$$

Interaction strengths are measured in units of

$$\Lambda_{jk} = \frac{\hbar^2}{2m_0^3 G \mathcal{T}} \lambda_{jk}. \quad (25)$$

We assume a Hubble parameter $H_0 = 70 \text{ km/s/Mpc}$ and matter density $\Omega_{m,0} = 0.3$. The density unit $\mathcal{M}/\mathcal{L}^3 = \rho_c$ is the critical density of the universe, and energy is measured in units of $\mathcal{M}\mathcal{L}^2\mathcal{T}^{-2}$.

Imaginary Time Solver

We find spherically symmetric ground states by solving the spherically symmetric versions of the GPP equations of motion in imaginary time and using the code units described above. The steps in our imaginary time evolution obey a “kick-drift-kick” algorithm (as in [38, 49, 51, 52]). Schematically, this can be represented for n iterations of

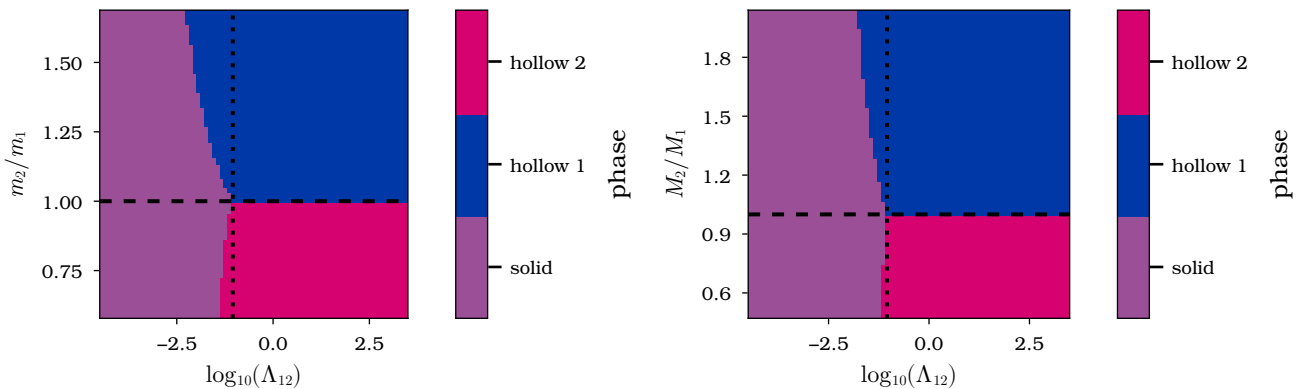


FIG. 3. Classification of spherically symmetric solutions found by relaxation in imaginary time, as a function of interaction strength Λ_{12} and particle mass ratio m_2/m_1 (**left**) and total mass ratio M_2/M_1 (**right**). Points are classified as “solid” if both fields have a local maximum at $r = r_{\min}$, or “hollow 1” (“hollow 2”) if ψ_1 (ψ_2) has local minimum at $r = r_{\min}$. The dotted line shows the analytic prediction $\Lambda_{12} = 0.09$ for the transition from solid to hollow states. The dashed line shows the expected separation between “hollow 1” and “hollow 2” states at $r_{s,1} = r_{s,2}$. In the **left** panel, all points have $M_1 = M_2 = 50M$ and $m_1 = m_0$; in the **right**, $M_1 = 50M$ and $m_1 = m_2 = m_0$.

timestep h for wavefunction i as:

$$\psi_i(t + nh) = \exp \left[-\frac{h}{2} V_{\text{eff}} \right] \quad (26)$$

$$\times \left(\prod_{j=1}^n \exp[hV_{\text{eff}}] \exp \left[-\frac{h}{2} \nabla^2 \right] \right) \quad (27)$$

$$\times \exp \left[\frac{h}{2} V_{\text{eff}} \right] \psi_i(t), \text{ where} \quad (28)$$

$$V_{\text{eff}} = m_i \Phi + \frac{1}{4} \sum_j m_j \lambda_{ij} |\psi_j|^2 \psi_i. \quad (29)$$

What the equations above don’t capture is that the gravitational potential Φ also gets updated at every timestep. Effectively, this is equivalent to n iterations of:

1. evolving ψ_i for a half-step $h/2$ in the gravitational potential $\Phi(t - \frac{h}{2})$,
2. applying the kinetic operator to ψ , then recalculating Φ from $\psi(t + \frac{h}{2})$,
3. evolving ψ_i for another half-step given the new Φ .
4. re-normalizing ψ_i so that the total mass in each field is conserved.

Additionally, **nSPIRa1** introduces a hard boundary at a given maximum radial distance $r = r_{\max}$. The boundary value of each field is fixed such that $r\psi_j|_{r=0} = r\psi_j|_{r=r_{\max}} = 0$; the latter is equivalent to specifying $\psi_j(r_{\max}) = 0$. We therefore take care to use only large enough r_{\max} such that $\psi_j(r_{\max}) \rightarrow 0$ for each field. In addition to r_{\max} , we must specify our grid size n_g , number of timesteps n , and initial conditions for the ψ_j profiles.

Though not central to our results in this paper, we have also produced ground state profiles assuming $\lambda = 0$ and

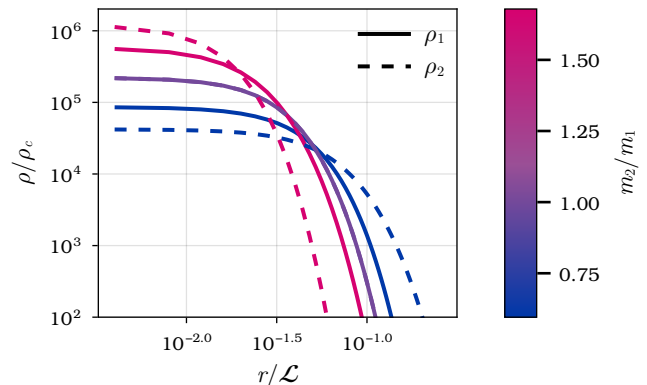


FIG. 4. Density profiles of nested solitons, computed by imaginary time relaxation in **nSPIRa1**. The solid lines denote ρ_1 and the dashed lines denote ρ_2 . The color scale denotes the ratio m_2/m_1 of the particle masses. In each case the total masses are $M_1 = M_2 = 50M$ and $\Lambda = 0$.

plotted it in Fig. 4 in order to verify that the behavior matches predictions in the literature.

-
- [1] E. G. M. Ferreira, *The Astronomy and Astrophysics Review* **29**, 7 (2021).
 - [2] A. H. Guth, *Phys. Rev. D* **23**, 347 (1981).
 - [3] A. D. Linde, *Phys. Lett. B* **108**, 389 (1982).
 - [4] A. Albrecht and P. J. Steinhardt, *Phys. Rev. Lett.* **48**, 1220 (1982).
 - [5] J. Martin, C. Ringeval, and V. Vennin, *Phys. Dark Univ.* **5-6**, 75 (2014), arXiv:1303.3787 [astro-ph.CO].
 - [6] W. Hu, R. Barkana, and A. Gruzinov, *Phys. Rev. Lett.* **85**, 1158 (2000).
 - [7] D. G. Levkov, A. G. Panin, and I. I. Tkachev, *Phys.*

- Rev. Lett. **121**, 151301 (2018), arXiv:1804.05857 [astro-ph.CO].
- [8] B. Eggemeier and J. C. Niemeyer, Phys. Rev. D **100**, 063528 (2019), arXiv:1906.01348 [astro-ph.CO].
- [9] K. Kirkpatrick, A. E. Mirasola, and C. Prescod-Weinstein, Phys. Rev. D **102**, 103012 (2020), arXiv:2007.07438 [hep-ph].
- [10] J. Chen, X. Du, E. W. Lentz, D. J. E. Marsh, and J. C. Niemeyer, Phys. Rev. D **104**, 083022 (2021), arXiv:2011.01333 [astro-ph.CO].
- [11] M. P. Hertzberg, E. D. Schiappacasse, and T. T. Yanagida, Phys. Rev. D **102**, 023013 (2020), arXiv:2001.07476 [astro-ph.CO].
- [12] K. Kirkpatrick, A. E. Mirasola, and C. Prescod-Weinstein, Phys. Rev. D **106**, 043512 (2022), arXiv:2110.08921 [hep-ph].
- [13] R. G. García, P. Brax, and P. Valageas, (2023), arXiv:2304.10221 [astro-ph.CO].
- [14] K.-Y. Su and P. Chen, Journal of Cosmology and Astroparticle Physics **2011**, 016 (2011).
- [15] L. Hui, J. P. Ostriker, S. Tremaine, and E. Witten, Phys. Rev. D **95**, 043541 (2017), arXiv:1610.08297 [astro-ph.CO].
- [16] H. Y. J. Chan, E. G. M. Ferreira, S. May, K. Hayashi, and M. Chiba, MNRAS **511**, 943 (2022), arXiv:2110.11882 [astro-ph.CO].
- [17] T. D. Yavetz, X. Li, and L. Hui, Phys. Rev. D **105**, 023512 (2022), arXiv:2109.06125 [astro-ph.CO].
- [18] E. Kendall, M. Gosenca, and R. Easther, Mon. Not. Roy. Astron. Soc. **526**, 1046 (2023), arXiv:2305.10340 [astro-ph.CO].
- [19] J. L. Zagorac, E. Kendall, N. Padmanabhan, and R. Easther, Phys. Rev. D **107**, 083513 (2023), arXiv:2212.09349 [astro-ph.CO].
- [20] B. Dave and G. Goswami, Journal of Cosmology and Astroparticle Physics **2023**, 015 (2023).
- [21] B. Dave and G. Goswami, Journal of Cosmology and Astroparticle Physics **2024**, 044 (2024).
- [22] S. Chakrabarti, B. Dave, K. Dutta, and G. Goswami, Journal of Cosmology and Astroparticle Physics **2022**, 074 (2022).
- [23] A. Arvanitaki, S. Dimopoulos, S. Dubovsky, N. Kaloper, and J. March-Russell, Phys. Rev. D **81**, 123530 (2010).
- [24] A. Arvanitaki and S. Dubovsky, Phys. Rev. D **83**, 044026 (2011).
- [25] N. Glennon, N. Musoke, and C. Prescod-Weinstein, Phys. Rev. D **107**, 063520 (2023), arXiv:2302.04302 [astro-ph.CO].
- [26] R. Easther, R. Flauger, and J. B. Gilmore, JCAP **04**, 027 (2011), arXiv:1003.3011 [astro-ph.CO].
- [27] N. Musoke, S. Hotchkiss, and R. Easther, Phys. Rev. Lett. **124**, 061301 (2020), arXiv:1909.11678 [astro-ph.CO].
- [28] S. C. Hotinli, J. Frazer, A. H. Jaffe, J. Meyers, L. C. Price, and E. R. M. Tarrant, Phys. Rev. D **97**, 023511 (2018), arXiv:1710.08913 [astro-ph.CO].
- [29] T.-L. Ho and V. B. Shenoy, Phys. Rev. Lett. **77**, 3276 (1996).
- [30] C. J. Myatt, E. A. Burt, R. W. Ghrist, E. A. Cornell, and C. E. Wieman, Phys. Rev. Lett. **78**, 586 (1997).
- [31] B. D. Esry, C. H. Greene, J. P. Burke, Jr., and J. L. Bohn, Phys. Rev. Lett. **78**, 3594 (1997).
- [32] E. Timmermans, Phys. Rev. Lett. **81**, 5718 (1998).
- [33] K. L. Lee, N. B. Jørgensen, I.-K. Liu, L. Wacker, J. J. Arlt, and N. P. Proukakis, Phys. Rev. A **94**, 013602 (2016).
- [34] X. Jiang, S. Wu, Q. Ye, and C. Lee, New Journal of Physics **21**, 023014 (2019).
- [35] E. M. Gutierrez, G. A. de Oliveira, K. M. Farias, V. S. Bagnato, and P. C. M. Castilho, Applied Sciences **11** (2021), 10.3390/app11199099.
- [36] J. C. Niemeyer, (2019), 10.1016/j.pnpnp.2020.103787, arXiv:1912.07064 [astro-ph.CO].
- [37] P.-H. Chavanis, Phys. Rev. D **84**, 043531 (2011).
- [38] N. Glennon and C. Prescod-Weinstein, Physical Review D **104**, 083532 (2021), arXiv:2011.09510 [astro-ph.CO].
- [39] N. L. Guo, *Ultralight Dark Matter Dynamics with an Absorbing Black Hole*, Master's thesis, University of Auckland (2020).
- [40] K. Blum and L. Teodori, Physical Review D **104**, 123011 (2021), arXiv:2105.10873 [astro-ph.CO].
- [41] P.-H. Chavanis, Phys. Rev. D **107**, 103503 (2023), arXiv:2211.13237 [gr-qc].
- [42] H.-Y. Schive, M.-H. Liao, T.-P. Woo, S.-K. Wong, T. Chiueh, T. Broadhurst, and W. Y. P. Hwang, Phys. Rev. Lett. **113**, 261302 (2014), arXiv:1407.7762 [astro-ph.GA].
- [43] M. Gosenca, A. Eberhardt, Y. Wang, B. Eggemeier, E. Kendall, J. L. Zagorac, and R. Easther, Phys. Rev. D **107**, 083014 (2023), arXiv:2301.07114 [astro-ph.CO].
- [44] H. N. Luu, P. Mocz, M. Vogelsberger, S. May, J. Borrow, S.-H. H. Tye, and T. Broadhurst, Monthly Notices of the Royal Astronomical Society **527**, 4162–4172 (2023).
- [45] H. Huang, H.-Y. Schive, and T. Chiueh, Monthly Notices of the Royal Astronomical Society **522**, 515 (2023), <https://academic.oup.com/mnras/article-pdf/522/1/515/49913421/stad998.pdf>.
- [46] F. van Dissel, M. P. Hertzberg, and J. Shapiro, Journal of Cosmology and Astroparticle Physics **2024**, 077 (2024).
- [47] H. N. Luu, P. Mocz, M. Vogelsberger, S. May, J. Borrow, S. H. H. Tye, and T. Broadhurst, (2023), 10.48550/ARXIV.2309.05694, arXiv:2309.05694 [astro-ph.CO].
- [48] J. L. Zagorac, I. Sands, N. Padmanabhan, and R. Easther, (2021), arXiv:2109.01920 [astro-ph.CO].
- [49] N. Musoke, Journal of Open Source Software **9**, 6035 (2024).
- [50] M. Jain, M. A. Amin, J. Thomas, and W. Wanichwecharungruang, (2023), arXiv:2304.01985 [astro-ph.CO].
- [51] F. Edwards, E. Kendall, S. Hotchkiss, and R. Easther, Journal of Cosmology and Astroparticle Physics **2018**, 027 (2018), arXiv:1807.04037 [astro-ph.CO].
- [52] N. Padmanabhan, E. Ronaghan, J. L. Zagorac, and R. Easther, in *2020 IEEE International Parallel and Distributed Processing Symposium Workshops (IPDPSW)* (2020) pp. 678–678.